

High-harmonic spectra of hexagonal nanoribbons from real-space time-dependent Schrödinger calculations

Helena Drüeke^a and Dieter Bauer^b

University of Rostock, Germany

Abstract. High-harmonic spectroscopy is a promising candidate for imaging electronic structures and dynamics in condensed matter by all-optical means and with unprecedented temporal resolution. We investigate harmonic spectra from finite, hexagonal nanoribbons, such as graphene and hexagonal boron nitride, in armchair and zig-zag configuration. The symmetry of the system explains the existence and intensity of the emitted harmonics.

1 Introduction

High-harmonic generation (HHG) has been first observed in gases [1,2]. Its non-perturbative nature, featuring a plateau of almost constant high-harmonic yield, was subsequently explained by the three-step model [3,4]: An electron is removed from the atom, propagates under the external field's influence, and recombines with the atom. The orbital energies of electrons in atoms do not depend on momentum, and the electron's dispersion relation in the continuum is shaped parabolically. Therefore, no harmonics are emitted from electrons in the ground state or free electrons, only by transitions between bound states or recombination from continuum states back to bound states.

To describe HHG in the bulk of solids, the orbital energies and the continuum are replaced by electronic bands [5]. This opens a whole new field of research [6,7,8,9,10,11,12,13]. Analogous to the HHG process in gases, the transition of electrons between valence and conduction bands causes high harmonics, called interband harmonics. Intraband harmonics, on the other hand, are produced by the movement of electrons in partially filled, non-parabolic bands. Band structures are usually defined for periodic or infinite solid bulk systems. However, every realistic system has boundaries, which may cause completely different HHG spectra compared to the bulk [14,15,16,17,18]. Graphene and hexagonal boron nitride (hBN) are two-dimensional materials that possess fascinating features with promising potential applications [19,20]. Their hexagonal structure allows for two different edges: zig-zag and armchair. While graphene consist only of carbon atoms (all identical), hBN is built from boron and nitrogen atoms. Recently, the interaction of intense laser light with graphene got

^a e-mail: helena.drueeke@uni-rostock.de

^b e-mail: dieter.bauer@uni-rostock.de

into the focus of interest for its prospects to steer electrons at will on ultrafast time scales [21, 22, 23, 24].

2 Methods

The nanoribbons' atomic nuclei were positioned in a hexagonal lattice, as described for the armchair and zig-zag configuration in the following sections 3 and 4. Atomic units are used throughout this paper unless stated otherwise. The distance between neighboring lattice sites was 2.683, the bond length in graphene (1.42 Å). An effective Pöschl-Teller potential $V(\mathbf{r}) = -\sum_i \frac{V_i}{\cosh^2(\varepsilon|\mathbf{r}-\mathbf{r}_i|)}$ with ion potentials $V_i = 3.2 \pm V_{\text{os}}$ and screening parameter $\varepsilon = 2$ describe the attractive potentials of the nuclei. For graphene ribbons, all atoms are carbon, therefore the additional on-site potential $V_{\text{os}} = 0$. A non-zero on-site potential represents two alternating, different kind of atoms, such as boron and nitrogen in hBN. At which lattice sites the ion potentials are increased or decreased by V_{os} is sketched in the following sections.

In this work, we did not employ the usual tight-binding approximation commonly made in condensed-matter theory but have developed a 2D, real-space, time-dependent Schrödinger solver for the *ab initio* simulation of the intense-laser interaction with 2D matter. In that way we are able to reveal differences and similarities in HHG spectra as compared to corresponding tight-binding studies, e.g., in Ref. [25]. The non-interacting electronic orbitals in our Schrödinger solver are defined on a two-dimensional grid of spacing $\Delta x = \Delta y = 0.2$, which encompasses all lattice sites plus a border of 8 on each side. In contrast to the usual tight-binding description, this allows us to have electron orbitals that are not only localized at lattice sites but also between them, or free electrons.

The electronic eigenstates of the system were found by imaginary-time propagation employing the Crank-Nicolson method [26]. Starting from a random initialization, imaginary timesteps $-0.05i$ are taken (each step followed by renormalization of the wavefunction) until the ground state is reached and the relative change of the state is smaller than the threshold of 10^{-18} for two consecutive iterations. To find the higher-lying states, the workflow is identical, but with an additional (Gram-Schmidt) orthogonalization to all previously found states in each iteration. This gives us all states of interest of the unperturbed system.

Real-time simulations of the interaction of all occupied electronic orbitals with a short laser pulse were performed with a timestep 0.05 using, again, Crank-Nicolson propagation. The pulse was a 4-cycle \sin^2 -shaped laser pulse of frequency $\omega = 0.0075$ ($\lambda \simeq 6.1 \mu\text{m}$) and polarized along the ribbon. The electronic dipoles were recorded at each time step during the laser pulse. Harmonic spectra were calculated as the absolute square of the Fourier transform of the recorded dipoles, multiplied by a symmetric Hann window [27, 28].

3 Armchair ribbon

First, we investigate a hexagonal nanoribbon in the armchair configuration. A total of 24 lattice sites are arranged in the shape of four hexagons as shown in Figure 1. For $V_{\text{os}} = 0$, the armchair ribbon is symmetric about the horizontal as well as the vertical axis through the center. The introduction of an on-site potential deepens the blue (square) sites' potentials while making the orange (circle) ones shallower. This causes a left-right asymmetry, while the top-bottom symmetry is conserved. Note that the lines drawn in Figure 1 connect nearest neighbors. In tight-binding calculations (such

as in Ref. [25]), hopping takes place along these lines. However, in our simulation based on the time-dependent Schrödinger equation, electronic wavefunctions are not restricted to move along these lines but may propagate in the entire plane.

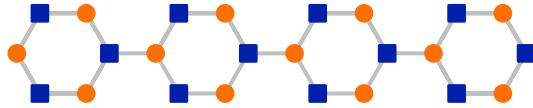


Fig. 1. Armchair ribbon: At the blue (square) lattice sites, the potential depth is increased by the on-site potential, $V_{\text{blue}} = V_{\text{avg}} + V_{\text{os}}$. The orange (circle) sites correspond to the shallower potentials of depth $V_{\text{orange}} = V_{\text{avg}} - V_{\text{os}}$.

The asymmetry in the potential leads to an asymmetry in the orbitals. Figure 2 (a-d) show the highest occupied (a and c) and lowest unoccupied (b and d) orbitals without (a and b) and with (c and d) on-site potential. The orbitals without on-site potential are horizontally and vertically symmetric (as is the potential), and there is only a small bandgap between the occupied and unoccupied states. With an on-site potential, the occupied orbitals are localized on the sites with deeper potentials and therefore have a decreased energy. The unoccupied orbitals are localized on the sites with shallower potentials and therefore have increased energy. This leads to a bandgap between the occupied and unoccupied orbitals, which, for $V_{\text{os}} \gtrsim 0.2$, grows linearly with the on-site potential (Figure 2 (e)). In contrast to tight-binding methods, our approach allows us to calculate an arbitrary number of orbitals of increasing energy. The next state above the conduction band is a "free" electron, i.e., not localized on the ribbon but still inside the simulation box with reflecting boundary conditions.

The incoming laser field is linearly polarized along the armchair ribbon. All emitted harmonics are linearly polarized in the same direction. The emission of harmonics polarized in the perpendicular direction requires a top-bottom asymmetry in the system, which the armchair ribbon does not possess, regardless of on-site potential. The bandwidths and bandgaps (ΔE_{intra} , ΔE_{min} , and ΔE_{max}) from Figure 2 (e) explain the most important features of the harmonic spectra shown in Figure 3. Intraband harmonics are only present at harmonic energies below the width of the valence band ΔE_{intra} . Interband harmonics can be observed between the minimum ΔE_{min} and maximum ΔE_{max} bandgap between the valence and (first) conduction band. Above the two bands are the box states (marked as gray lines in Figure 2 (e)), which are not localized on the ribbon, and whose energies are determined by the size of the simulation box. Only the energies of the four lowest box states are shown, but many more lie above them. Transitions to these box states cause harmonics above ΔE_{max} . In an experiment, there are no box states (unless it is performed in a cavity), but transitions to higher bands or the continuum would also cause harmonics beyond the maximum bandgap. These can not be described in tight-binding approximation with one atomic orbital per site because then the energy difference between states is bound from above by ΔE_{max} (see Ref. [25]).

4 Zig-zag ribbon

In the zig-zag configuration, a total of 26 lattice sites are arranged in six hexagons, as shown in Figure 4. On the orange sites, the on-site potential decreases the potential

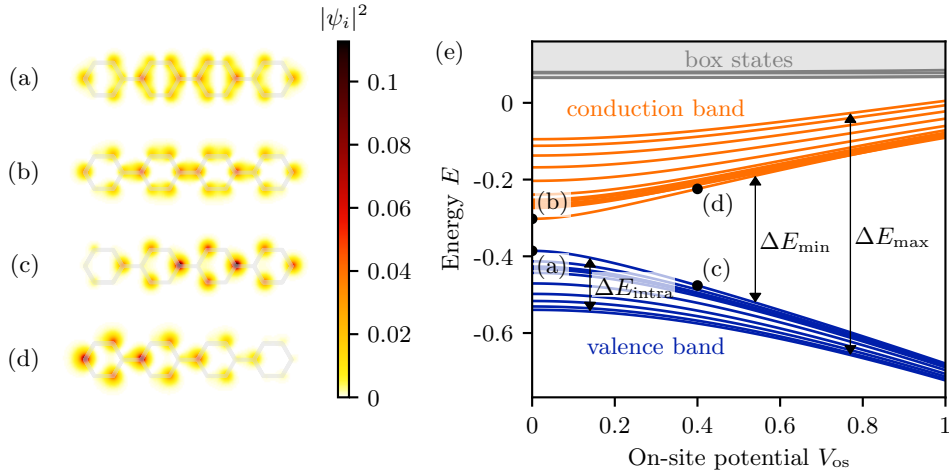


Fig. 2. Orbitals and orbital energies of the armchair ribbon. (a) - (d) Orbitals of the armchair ribbon. (a) Highest occupied orbital without on-site potential ($V_{os} = 0$). (b) Lowest unoccupied orbital without on-site potential ($V_{os} = 0$). (c) Highest occupied orbital with on-site potential $V_{os} = 0.4$. (d) Lowest unoccupied orbital with on-site potential $V_{os} = 0.4$. (e) Orbital energies of the armchair ribbon as a function of on-site potential V_{os} . The orbital energies of the orbitals shown in (a) - (d) are marked. The arrows mark the bandwidth of the valence band (ΔE_{intra}) and the minimum and maximum bandgap between the valence and (first) conduction band (ΔE_{min} and ΔE_{max}).

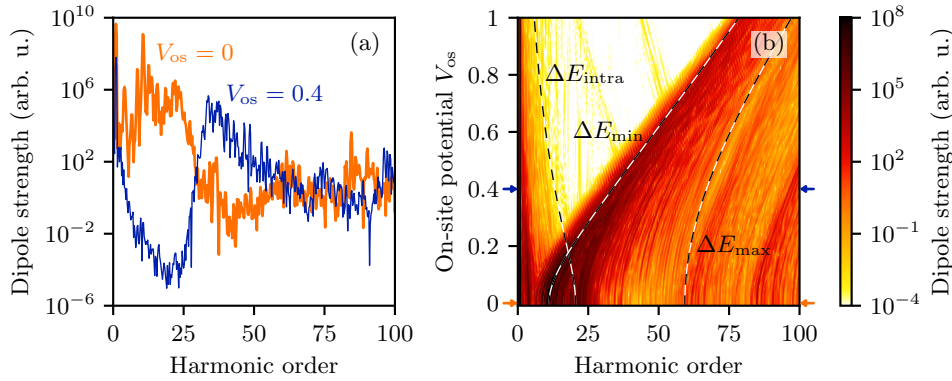


Fig. 3. Harmonic spectra of the armchair ribbon in parallel direction. (a) Harmonic spectra without (bold orange line, $V_{os} = 0$) and with (blue line, $V_{os} = 0.4$) on-site potential. (b) Harmonic spectra as a function of harmonic order and on-site potential.

depth, while on the blue sites, it deepens the potential. The on-site potential causes a top-bottom asymmetry but no left-right asymmetry.

As for the armchair ribbon, the asymmetry of the potential leads to decreased energies of states in the valence band, localized at the deeper sites, and increased energies of states in the conduction bands, localized at the shallower sites (see Figure 5). The minimum bandgap increases almost linearly with the on-site potential, the bandwidths of both bands decrease.

The parallelly polarized harmonics (Figure 6 (a)) are present with and without on-site potential. The bandwidth and bandgaps can explain the cutoffs of both intra- and interband harmonics. Perpendicular harmonics (Figure 6 (b)) with on-site potential

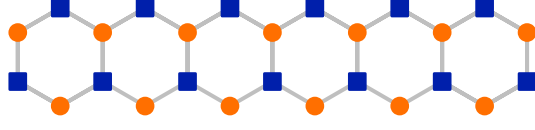


Fig. 4. Zig-zag ribbon: At the blue (square) lattice sites, the potential depth is increased by the on-site potential, $V_{\text{blue}} = V_{\text{avg}} + V_{\text{os}}$. The orange (circle) sites correspond to the shallower potentials of depth $V_{\text{orange}} = V_{\text{avg}} - V_{\text{os}}$.

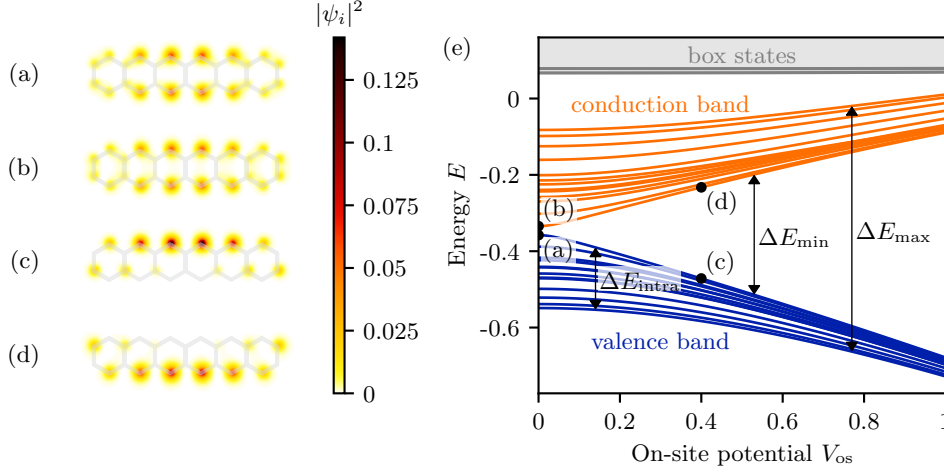


Fig. 5. Orbitals and orbital energies of the zig-zag ribbon. (a) - (d) Orbitals of the zig-zag ribbon. (a) Highest occupied orbital without on-site potential ($V_{\text{os}} = 0$). (b) Lowest unoccupied orbital without on-site potential ($V_{\text{os}} = 0$). (c) Highest occupied orbital with on-site potential $V_{\text{os}} = 0.4$. (d) Lowest unoccupied orbital with on-site potential $V_{\text{os}} = 0.4$. (e) Orbital energies of the zig-zag ribbon as a function of on-site potential V_{os} . The orbital energies of the orbitals shown in (a) - (d) are marked. The arrows mark the bandwidth of the valence band (ΔE_{intra}) and the minimum and maximum bandgap between the valence and (first) conduction band (ΔE_{min} and ΔE_{max}).

agree with these cutoffs, as well. Without an on-site potential, there is no top-bottom asymmetry, and therefore almost no harmonics perpendicular to the laser are observed. Transitions to the box states lead to weak harmonic emission above ΔE_{max} .

5 Conclusion

The introduction of an on-site potential in hexagonal nanoribbons causes lower energies for occupied states and higher energies for unoccupied states. The valence band's bandwidth decreases, and the minimum and maximum bandgaps between the valence and conduction bands increase. These three energies explain the overall features in harmonic spectra for different on-site potentials. Intraband harmonics are only present at energies below the valence bandwidth. Interband harmonics are present at energies between the minimum and maximum bandgap. For a laser polarized along the ribbon, the resulting harmonics are polarized in the same direction unless a non-zero on-site potential causes a top-bottom asymmetry, which is only possible in the zig-zag ribbon.

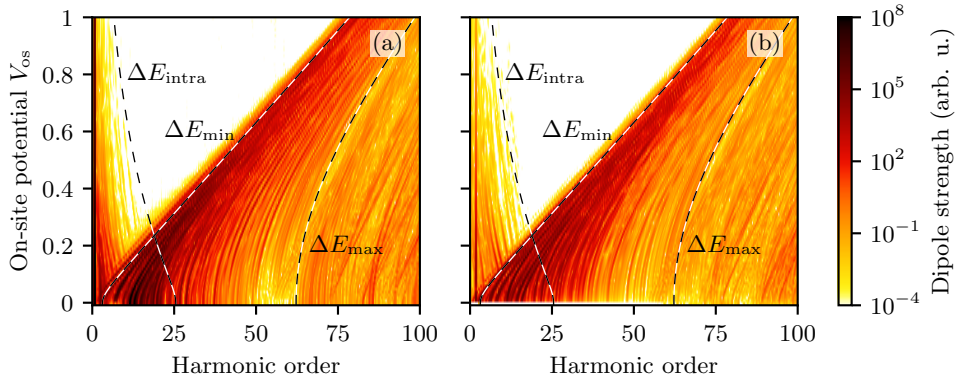


Fig. 6. Harmonic spectra of the zig-zag ribbon as a function of on-site potential in (a) parallel and (b) perpendicular polarization.

The results of this paper provide valuable verification of simpler tight-binding models [25]. Our approach is not limited to a fixed number of states (grouped in bands), and our results account for transitions to even higher bands or the continuum. However, these transitions are expected to play an important role only in the generation of higher harmonics beyond the cutoff ΔE_{\max} , leading to higher-order plateaus with decreasing yield (see, e.g., [29]). On the other hand, tight-binding approaches capture the essential mechanisms underlying high-harmonic generation up to ΔE_{\max} , are computationally much less demanding and thus can be used to investigate much larger systems.

The datasets generated and analyzed during this study are available at doi:10.17605/OSF.IO/8RTFU [30].

References

1. A. McPherson, G. Gibson, H. Jara, U. Johann, T. S. Luk, I. A. McIntyre, K. Boyer, and C. K. Rhodes, “Studies of multiphoton production of vacuum-ultraviolet radiation in the rare gases,” *J. Opt. Soc. Am. B, JOSAB*, vol. 4, pp. 595–601, Apr. 1987. Publisher: Optical Society of America.
2. M. Ferray, A. L’Huillier, X. F. Li, L. A. Lompre, G. Mainfray, and C. Manus, “Multiple-harmonic conversion of 1064 nm radiation in rare gases,” *J. Phys. B: At. Mol. Opt. Phys.*, vol. 21, pp. L31–L35, Feb. 1988.
3. P. B. Corkum, “Plasma perspective on strong field multiphoton ionization,” *Physical Review Letters*, vol. 71, pp. 1994–1997, Sept. 1993.
4. M. Lewenstein, P. Balcou, M. Y. Ivanov, A. L’Huillier, and P. B. Corkum, “Theory of high-harmonic generation by low-frequency laser fields,” *Physical Review A*, vol. 49, pp. 2117–2132, Mar. 1994.
5. G. Vampa and T. Brabec, “Merge of high harmonic generation from gases and solids and its implications for attosecond science,” *Journal of Physics B: Atomic, Molecular and Optical Physics*, vol. 50, p. 083001, Apr. 2017.
6. S. Ghimire, A. D. DiChiara, E. Sistrunk, P. Agostini, L. F. DiMauro, and D. A. Reis, “Observation of high-order harmonic generation in a bulk crystal,” *Nature Physics*, vol. 7, pp. 138–141, Feb. 2011.
7. S. Ghimire, A. D. DiChiara, E. Sistrunk, G. Ndabashimiye, U. B. Szafruga, A. Mohammad, P. Agostini, L. F. DiMauro, and D. A. Reis, “Generation and propagation of high-order harmonics in crystals,” *Physical Review A*, vol. 85, p. 043836, Apr. 2012.

8. S. Ghimire, G. Ndabashimiye, A. D. DiChiara, E. Sistrunk, M. I. Stockman, Pierre Agostini, L. F. DiMauro, and D. A. Reis, “Strong-field and attosecond physics in solids,” *Journal of Physics B: Atomic, Molecular and Optical Physics*, vol. 47, no. 20, p. 204030, 2014.
9. M. Hohenleutner, F. Langer, O. Schubert, M. Knorr, U. Huttner, S. W. Koch, M. Kira, and R. Huber, “Real-time observation of interfering crystal electrons in high-harmonic generation,” *Nature*, vol. 523, pp. 572–575, July 2015.
10. G. Ndabashimiye, S. Ghimire, M. Wu, D. A. Browne, K. J. Schafer, M. B. Gaarde, and D. A. Reis, “Solid-state harmonics beyond the atomic limit,” *Nature*, vol. 534, pp. 520–523, June 2016.
11. T. Ikemachi, Y. Shinohara, T. Sato, J. Yumoto, M. Kuwata-Gonokami, and K. L. Ishikawa, “Trajectory analysis of high-order-harmonic generation from periodic crystals,” *Physical Review A*, vol. 95, p. 043416, Apr. 2017.
12. Y. S. You, Y. Yin, Y. Wu, A. Chew, X. Ren, F. Zhuang, S. Gholam-Mirzaei, M. Chini, Z. Chang, and S. Ghimire, “High-harmonic generation in amorphous solids,” *Nature Communications*, vol. 8, p. 724, Dec. 2017.
13. C. Yu, K. K. Hansen, and L. B. Madsen, “High-order harmonic generation in imperfect crystals,” *Phys. Rev. A*, vol. 99, p. 063408, June 2019.
14. D. Bauer and K. K. Hansen, “High-Harmonic Generation in Solids with and without Topological Edge States,” *Physical Review Letters*, vol. 120, Apr. 2018.
15. H. Drüeke and D. Bauer, “Robustness of topologically sensitive harmonic generation in laser-driven linear chains,” *Phys. Rev. A*, vol. 99, p. 053402, May 2019.
16. C. Jürß and D. Bauer, “High-harmonic generation in Su-Schrieffer-Heeger chains,” *Physical Review B*, vol. 99, May 2019.
17. K. K. Hansen, D. Bauer, and L. B. Madsen, “Finite-system effects on high-order harmonic generation: From atoms to solids,” *Physical Review A*, vol. 97, p. 043424, Apr. 2018.
18. A. Chacón, W. Zhu, S. P. Kelly, A. Dauphin, E. Pisanty, D. Kim, D. E. Kim, A. Picón, C. Ticknor, M. F. Ciappina, A. Saxena, and M. Lewenstein, “Observing Topological Phase Transitions with High Harmonic Generation,” *arXiv:1807.01616 [cond-mat, physics:quant-ph]*, Jan. 2020. arXiv: 1807.01616.
19. A. H. Castro Neto, F. Guinea, N. M. R. Peres, K. S. Novoselov, and A. K. Geim, “The electronic properties of graphene,” *Rev. Mod. Phys.*, vol. 81, pp. 109–162, Jan. 2009. Publisher: American Physical Society.
20. J. Wang, F. Ma, and M. Sun, “Graphene, hexagonal boron nitride, and their heterostructures: properties and applications,” *RSC Adv.*, vol. 7, no. 27, pp. 16801–16822, 2017.
21. H. Koochaki Keldarreh, V. Apalkov, and M. I. Stockman, “Graphene superlattices in strong circularly polarized fields: Chirality, Berry phase, and attosecond dynamics,” *Physical Review B*, vol. 96, p. 075409, Aug. 2017.
22. T. Higuchi, C. Heide, K. Ullmann, H. B. Weber, and P. Hommelhoff, “Light-field-driven currents in graphene,” *Nature*, vol. 550, pp. 224–228, Oct. 2017.
23. C. Heide, T. Higuchi, H. B. Weber, and P. Hommelhoff, “Coherent Electron Trajectory Control in Graphene,” *Physical Review Letters*, vol. 121, Nov. 2018.
24. M. Baudisch, A. Marini, J. D. Cox, T. Zhu, F. Silva, S. Teichmann, M. Massicotte, F. Koppens, L. S. Levitov, F. J. García de Abajo, and J. Biegert, “Ultrafast nonlinear optical response of Dirac fermions in graphene,” *Nature Communications*, vol. 9, Dec. 2018.
25. C. Jürß and D. Bauer, “High-order harmonic generation in hexagonal nanoribbons,” *arXiv:2101.02961 [cond-mat, physics:physics, physics:quant-ph]*, Jan. 2021. arXiv: 2101.02961.
26. D. Bauer (ed.), *Computational Strong-Field Quantum Dynamics: Intense Light-Matter Interactions*. De Gruyter Textbook, De Gruyter, 2017.
27. J. C. Baggesen and L. B. Madsen, “On the dipole, velocity and acceleration forms in high-order harmonic generation from a single atom or molecule,” *Journal of Physics B: Atomic, Molecular and Optical Physics*, vol. 44, no. 11, p. 115601, 2011.

28. F. J. Harris, “On the use of windows for harmonic analysis with the discrete Fourier transform,” *Proceedings of the IEEE*, vol. 66, pp. 51–83, Jan. 1978.
29. K. K. Hansen, T. Deffge, and D. Bauer, “High-order harmonic generation in solid slabs beyond the single-active-electron approximation,” *Physical Review A*, vol. 96, p. 053418, Nov. 2017.
30. H. Drüeke and D. Bauer, “High-harmonic spectra of hexagonal nanoribbons from real-space time-dependent Schrödinger calculations: data repository,” Jan. 2021.